Research Article Vol. 34, No. 3 / 9 Feb 2026 / Optics Express 5102
Optics EXPRESS

Comprehensive spatial and temporal analysis of attosecond time-resolved photoemission dynamics

KAI LIU,[1] FENG WANG,[1] QING LIAO,[1,*] WEI CAO,[2] PEIXIANG LU,[1,2] AND UWE THUMM[3]

[1]Hubei Key Laboratory of Optical Information and Pattern Recognition, Wuhan Institute of Technology, Wuhan 430205, China
[2]Wuhan National Laboratory for Optoelectronics and School of Physics, Huazhong University of Science and Technology, Wuhan 430074, China
[3]Department of Physics, Kansas State University, Manhattan, KS 66506, USA
*liaoqing@wit.edu.cn

Abstract: Attosecond time-resolved photoemission spectroscopy (ATRPS) holds great potential for simultaneous high-resolution imaging of XUV pump fields, laser probe fields, and target initial quantum states, yet this potential remains largely untapped, since current studies only extract integral metrics (e.g., photoemission times) from three-dimensional spectrograms, discarding valuable spatial-temporal-energetic differential information, while reconstruction algorithms often neglect critical Coulomb-laser coupling effects. To address this deficiency, we develop a quantum path-integral (QPI) model tailored for ATRPS, adopting a velocity-gauge formalism that rigorously captures the photoelectron phase dynamics and employing retroactive path tracing to avoid omitting critical quantum paths. The model reveals the joint distribution of absorbed XUV photon energy, ionization time, and the initial electron position for photoelectrons with fixed final kinetic energy. This distribution coherently couples XUV pump field spectral features, laser probe field temporal dynamics, and initial state probability density. Crucially, the QPI model unifies streaking and RABBIT (both derive emission times from path phase differences), enables efficient time extraction at any relative delay τ, and images with attosecond-picometer resolution the three foundamental quanties, XUV pump fields, laser probe fields, and target initial quantum states. The QPI model effectively utilizes previously overlooked photoelectron differential information, transforming ATRPS from simple integral analysis into a multi-parameter high-resolution imaging tool, and providing a physical model for an advanced reconstruction algorithms.

1. Introduction

Attosecond time-resolved photoemission spectroscopy (ATRPS) enables direct probing of photoelectron emission time delays on the attosecond timescale, with sub-attosecond precision [1–9]. This breakthrough allows for real-time observation of ultrafast quantum dynamical processes at the atomic scale [1,2,10–13]. By leveraging ATRPS techniques, such as attosecond streaking and the reconstruction of attosecond beating by interference of two-photon transitions (RABBIT) [1,2,10,11], researchers have successfully measured the Wigner time delay during atomic photoionization, unveiling the scattering phase dynamics of electron wave packets in the ionic field [12]. However, photoionization processes in molecular systems pose substantial challenges, both experimentally [14–17] and theoretically [18–21]. These challenges stem from the intricate anisotropic potential fields, degeneracy of electronic states, and, for molecular targets, additional nuclear degrees of freedom. The electron density distribution and orbital asymmetry

#586214 https://doi.org/10.1364/OE.586214
Journal © 2026 Received 28 Nov 2025; revised 19 Jan 2026; accepted 19 Jan 2026; published 3 Feb 2026

Optics EXPRESS

give rise to a marked orientation-dependence in photoemission time delays [18,22]. Additionally, they are accompanied by characteristics of electron localization [23,24].

Extensive efforts have been dedicated to measuring and interpreting photoemission time delays. These time delays are typically derived by integrating attosecond time-resolved photoelectron spectrograms over energy and extracting the temporal shifts relative to a reference. However, differential information about the photoemission dynamics, encoded in three-dimensional spectrograms, is often discarded during this integration process. In single-photon ionization, photoelectrons originating from the same bound state acquire identical final kinetic energy upon absorbing photons of equal energy, regardless of their ionization time or initial position. Consequently, numerous differential characteristics, such as the initial state probability density and the precise form of the driving field, are convolved into kinetic energy spectra and cannot be recovered from such integrated data.

Notably, this limitation can be addressed by dressing photoelectrons with a weak probe laser field and scanning the relative delay τ between the extreme ultraviolet (XUV) pump and probe laser field. Through this approach, the aforementioned differential information is unambiguously encoded in attosecond time-resolved spectrograms. This is because, in the presence of the Coulomb field, the energy transfer between photoelectrons and the probe field–and thus the spectrogram itself–depends on ionization time, initial position, and τ [25,26]. These variables are directly linked to the pump field, probe field, and initial state. As a result, higher-order moments of time-resolved photoelectron spectrograms (i.e., RABBIT and streaking "traces" [27]) can reveal substantially more information than spectrally integrated photoemission time delays. Despite the significant attention paid to integrally extracted photoemission times, these distributed pieces of information have often been overlooked.

Furthermore, despite substantial progress in explaining photoemission time delays [4,8,9,13,26, 28–33], no comprehensive model capable of simulating various types of attosecond time-resolved photoelectron spectrograms at a quantitative level comparable to full quantum models exists. A deeper understanding of strong-field photoelectron dynamics frequently relies on semiclassical models, including the strong-field approximation (SFA) [34–36], Coulomb-corrected SFA [37–39], Coulomb quantum-orbit SFA (CQSFA) [40,41], quantum trajectory Monte Carlo (QTMC) [42] and semiclassical two-step (SCTS) models [43], action calculations by classical trajectory integration in varying electromagnetic fields [44,45], and adiabatic models for strong-field photoelectron holography [46,47]. These models can identify underlying mechanisms and provide satisfactory simulations of photoelectron spectra in terms of photoelectron trajectories. Within these frameworks, accurately describing the photoelectron phase is critical for understanding the mechanisms responsible for spectral features in strong-field ionization. However, the computation of the photoelectron phase varies across these models, and the extent to which they accurately account for this phase remains unclear, primarily because the initial conditions of electrons following highly nonlinear photoexcitation (e.g., initial momentum distribution and distortion of the initial state by strong laser fields) are too complex to model precisely.

The photoemission time is inherently linked to the phase of the corresponding final continuum state, which is periodically modulated by τ. More specifically, the photoemission time delay depends linearly on the unmodulated component of this phase. Only for sufficiently weak probe pulses, this component remains independent of τ, as streaking traces become distorted at high probe field strengths [28]. Thus, ATRPS provides direct access to photoelectron phase differences with unprecedented accuracy. It provides an ideal benchmark for verifying the accuracy of the photoelectron phase in semiclassical models, since single-photon excitation represents the simplest form of photoexcitation.

To address these challenges, we develop an advanced **quantum path-integral (QPI) model** (Fig. 1) tailored for ATRPS, building upon our prior velocity-gauge QPI framework [26]. This work introduces two fundamental methodological improvements: (1) a gauge-transformed phase

Optics EXPRESS

derivation rigorously derived from the classical action via a canonical transformation, and (2) a deterministic retroactive path tracing strategy that systematically identifies all quantum paths contributing to a given final momentum. These innovations overcome the limitations of our previous approximation [26], where photoelectron phases were represented as the sum of Volkov and Coulomb-laser coupling terms with randomly sampled initial positions. In attosecond time-resolved photoemission, an XUV attosecond pump pulse selectively excites electrons from bound states to continuum states, while (for direct emission leaving the residual ion in the ground state) a weak probe laser pulse modulates photoelectron propagation and energy transfer without noticeably perturbing the initial bound state. For sufficiently weak probe fields (with peak intensities ranging from 5×10^{10} to 2×10^{11} W/cm^2), the photoemission time delay varies by less than 0.1 attoseconds, ensuring the hydrogen ground state remains undisturbed. Under such conditions, first-order perturbation theory accurately describes the initial propagation of single-photon-excited electrons. This framework allows direct validation against exact time-dependent Schrödinger equation (TDSE) simulations, focusing on benchmarking phase representations in semiclassical models and identifying the most physically consistent path descriptions. We note that for shake-up ionization (leaving the residual ion in an excited state) even weak laser probe fields significantly affect the residual-ion charge distribution and thereby the photoelectron phase [4,9].

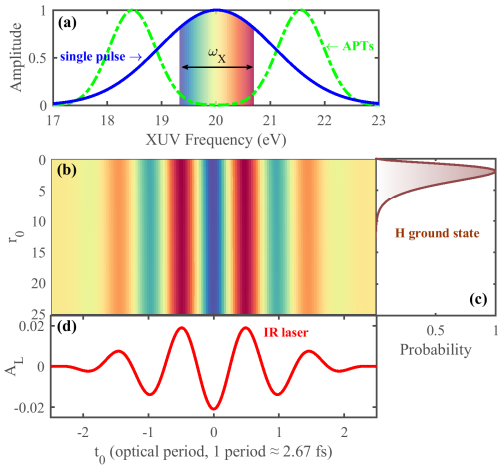

Fig. 1. Compilation of core physical quantities in the QPI Model. (a) XUV frequency amplitude distributions for a single attosecond pulse (blue solid line) and APTs (green dashed line). The XUV frequency is shifted by the initial-state binding energy ϵ_i to align with the final photoelectron kinetic energies, corresponding to the energy conservation relation $\omega_X = p_0^2/2 + V(r_0) - \epsilon_i$. (b) Joint distribution of the absorbed XUV photon energy ω_X (color bar as in panel (a) for the central region of the XUV pulse), photoionization time t_0, and initial position r_0 for photoelectrons with a final kinetic energy of 20 eV. This distribution illustrates the coherent coupling of ω_X (XUV pump field spectrum), t_0 (temporal features of the laser probe field), and r_0 (initial-state spatial distribution) in the QPI model. (c) Normalized radial probability density of the initial hydrogen atom ground state. Its weighting effect on quantum paths determines the transition amplitude (Eq. (2)). (d) Probe laser potential $A_L(t_0)$ for a 5 fs, 800 nm laser pulse with an intensity of 5×10^{10} W/cm^2. Its correlation with t_0 determines the efficiency of energy transfer between photoelectrons and the laser field ($\epsilon_{CL} \propto A_L(t_0)$).

The QPI model's core strengths lie in its **computational efficiency** and **multidimensional interpretability**:

Optics EXPRESS

1. **Retroactive path tracing**: By working backward from a given final momentum to identify all contributing initial conditions, it avoids the exhaustive forward sampling of traditional semiclassical models (e.g., QTMC, SCTS), drastically reducing computational overhead while ensuring no critical quantum paths are omitted.

2. **Quantitative precision**: It achieves excellent agreement with TDSE calculations in simulating attosecond streaking and RABBIT spectrograms (Figs. 2–3), capturing subtle Coulomb-laser field coupling effects. Notably, the photoemission times calculated by the QPI model show excellent agreement with TDSE results. Even at very low photoelectron energies, the discrepancy remains within 1 attosecond, markedly surpassing the performance of a classical model (Fig. 4) which neglects quantum phase effects.

3. **Simplified time extraction**: Photoemission time delays are directly derived from phase differences between interfering wave packets, eliminating the need for time-consuming spectrogram simulation and subsequent integration [Fig. 4(b)].

4. **Spatio-temporal mapping**: It unveils the joint distribution of absorbed XUV photon energy, ionization time, and initial position for photoelectrons of a given final kinetic energy (Fig. 5), which coherently encode the pump field spectrum, probe field dynamics, and initial state probability density, relating three-dimensional (3D) spectrograms to three fundamental physical quantities.

5. **Unified framework for streaking and RABBIT**: By revealing that the photoemission time delays measured by both techniques are fundamentally defined by the τ-independent phase difference between two interfering photoelectron channels [Figs. 4(b), 6], it explains why their extracted photoemission time delays coincide. This unifies the “classical clock" (streaking) and “quantum clock" (RABBIT) paradigms under a single theoretical umbrella, as both techniques ultimately quantify the same intrinsic electron emission time encoded in the quantum phase interference.

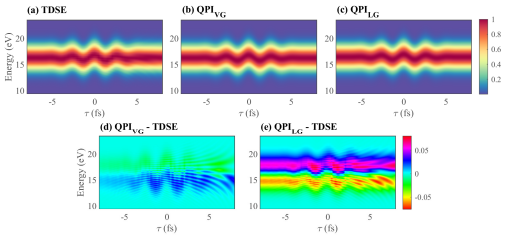

Fig. 2. Normalized attosecond time-resolved photoelectron spectrograms of hydrogen atoms: TDSE vs. QPI Model (velocity/length gauges). Hydrogen atoms are ionized by a 500 as, 30 eV XUV pump pulse and probed by a 5 fs, 800 nm, 5×10^{10} W/cm^2 laser pulse. Results are presented for: (a) TDSE simulations; (b) the QPI model in velocity gauge; (c) the QPI model in length gauge. Panels (d) and (e) show the residual differences between QPI results (velocity gauge and length gauge, respectively) and TDSE results.

Optics EXPRESS

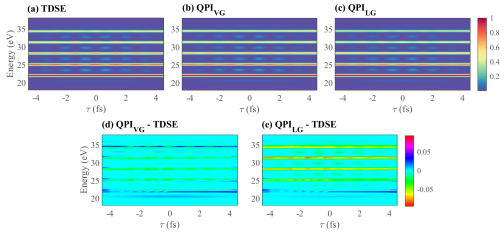

Fig. 3. Normalized attosecond time-resolved photoelectron spectrograms of hydrogen atoms: TDSE vs. QPI Model (velocity/length gauges). Hydrogen atoms are ionized by APTs with five high-order harmonics (lowest harmonic at 35.7 eV) and probed by a 5 fs, 800 nm, 5×10^{10} W/cm^2 laser pulse. Results are presented for: (a) TDSE simulations; (b) the QPI model in velocity gauge; (c) the QPI model in length gauge. Panels (d) and (e) show the residual differences between QPI results (velocity gauge and length gauge, respectively) and TDSE results.

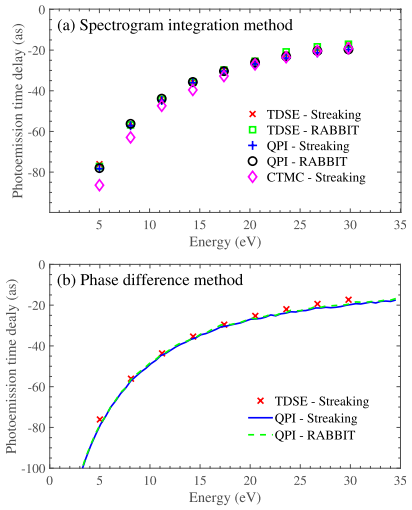

Fig. 4. Photoemission time delays for hydrogen atoms: extraction methods and model validation. (a) Photoemission time delays extracted via the spectrogram integration method, a traditional approach relying on energy integration of spectrograms and temporal shift analysis. Results include: TDSE simulations for streaking (red crosses) and RABBIT (green squares); the QPI model (velocity gauge) for streaking (blue plus signs) and RABBIT (black open circles); and CTMC simulations for streaking (purple diamonds). The QPI model shows excellent agreement with the TDSE results across all energies, while CTMC deviates significantly at low energies (due to neglect of quantum phase effects). (b) Photoemission times derived via the phase difference method, a QPI model-specific efficient approach, calculated from the τ-independent phase difference $\Delta\Phi$ between interfering quantum paths. Results include the QPI model (velocity gauge) for streaking (blue solid lines) and RABBIT (green dashed lines) settings, with TDSE streaking results from panel (a) shown for comparison. This method eliminates time-consuming full spectrogram simulations while maintaining complete consistency with TDSE results. It reveals that streaking and RABBIT, despite using distinct XUV sources, essentially measure photoemission time delays via the same physical mechanism, unifying the two techniques.

Optics EXPRESS

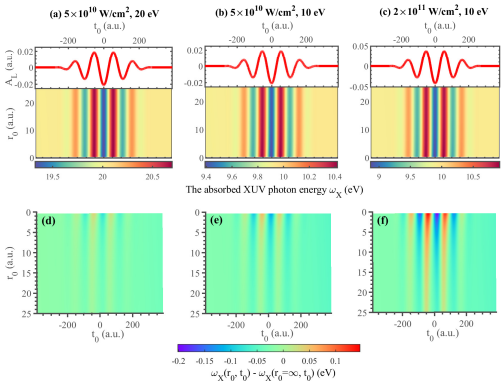

Fig. 5. (a)-(c) Joint distributions of absorbed XUV photon energy ω_X (shifted by the initial-state binding energy ϵ_i to align with the final kinetic energies of the photoelectrons), photoionization time t_0, and initial position r_0 for photoelectrons with different final kinetic energies and laser intensities: (a) 20 eV final kinetic energy, 5×10^{10} W/cm^2; (b) 10 eV, 5×10^{10} W/cm^2; (c) 10 eV, 2×10^{11} W/cm^2. These distributions visualize the QPI model's core insight: ω_X, t_0, and r_0 coherently couple the XUV pump field spectrum, probe laser field temporal dynamics [via $A_L(t_0)$], and initial state probability density, sampling distinct XUV spectral segments. (d)-(f) Residual differences between the joint distributions in (a)-(c) and their counterparts where initial state probability density and Coulomb potential are neglected ($r_0 = \infty$). These residuals quantify the critical role of Coulomb-laser coupling, which is more pronounced closer to the nucleus, for lower kinetic energies (10 eV vs. 20 eV), and at higher laser intensities. Laser vector potentials are included for comparison, linking t_0 distributions to the probe field's temporal modulation of the energy transfer.

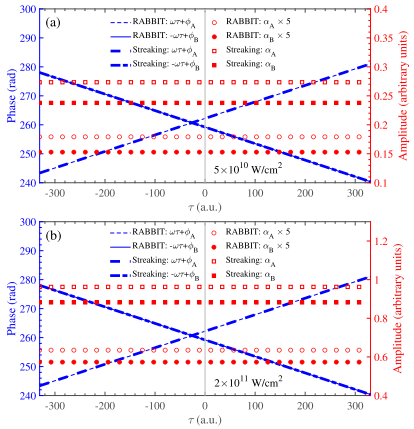

Fig. 6. The phase (left) and amplitude (right) of two coherent quantum path channels (A: IR photon emission, B: laser photon absorption) for photoelectrons with 20 eV final kinetic energy for streaking and RABBIT at laser intensities of (a) 5×10^{10} W/cm^2 and (b) 2×10^{11} W/cm^2. Notably, despite their distinct XUV sources (streaking: single attosecond pulse with continuous spectrum; RABBIT: attosecond pulse train with discrete high-order harmonics), the phases of channels A/B for streaking and RABBIT exactly coincide. This is a key QPI model prediction that reveals their shared physical origin: both techniques quantify photoemission time delays via the same τ-independent phase difference ($\Delta\Phi = \Phi_B - \Phi_A < 0$, as indicated by the vertical lines at $\tau = 0$) of interfering quantum paths. In contrast, increasing laser intensity enhances the amplitudes of channels A/B, but does not alter their phases, further validating the laser-intensity independence of photoemission time delays.

Optics EXPRESS

2. Method

To theoretically describe the attosecond time-resolved photoemission dynamics and overcome the limitations of traditional semiclassical models, we develop the QPI model and complement it with a tailored numerical algorithm. The model establishes the theoretical framework for tracing the photoelectron dynamics, while the numerical approach enables precise implementation of this framework.

2.1. QPI model

The QPI model is designed to systematically describe the coherent dynamics of photoelectrons, including their transition amplitude, phase evolution, and coupling to Coulomb and laser fields. This framework provides a rigorous theoretical foundation for interpreting attosecond time-resolved spectrograms by explicitly incorporating spatial and temporal information.

2.1.1. Transition amplitude and phase dynamics

The core of the QPI model lies in its formulation of the photoelectron transition amplitude, which quantifies the probability of an electron being excited from an initial bound state to a continuum state with asymptotic momentum $\vec{p}_f$ under the action of an XUV pump field $\vec{E}_X$ and a laser probe field [13,27,48]. For photoelectrons with asymptotic momentum $\vec{p}_f$, the transition amplitude is defined as (atomic units are used unless otherwise specified)

$$T(\vec{p}_f,\tau) \propto \int \left\langle \frac{1}{r_0} e^{-i\Phi(\vec{p}_f,\vec{r}_0,t_0)} \mid \vec{E}_X(t_0+\tau)\cdot\vec{r}_0 \mid \Psi_i(\vec{r}_0,t_0) \right\rangle dt_0, \tag{1}$$

where $\Phi(\vec{p}_f,\vec{r}_0,t_0)$ is the photoelectron phase, encoding the dynamics of electron wave packets along classical trajectories in the coupled Coulomb-laser field. These trajectories are sampled across two independent temporal and spatial dimensions: the photoionization time t_0 (marking the instant of electron ionization by the XUV pulse) and the initial position $\vec{r}_0$ (indicating the spatial point where the electron is released). This sampling ensures that spatial and temporal details of the photoemission process are preserved.

To validate the model, its predictions are compared with exact results from 3D TDSE simulations [26]. For linearly polarized fields, photoemission along the polarization direction simplifies to a half-scattering process that solely depends on the magnitude of the asymptotic photoelectron momentum p_f [13,29,30] and reduces the amplitude to

$$T(p_f,\tau) \propto \iint r_0^2 e^{i\Phi(p_f,r_0,t_0)} E_X(t_0+\tau)\Psi_i(r_0,t_0)dt_0dr_0. \tag{2}$$

The initial state of hydrogen atoms (used here as a benchmark) is $\Psi_i(r_0,t_0) = e^{-r_0-i\epsilon_i t_0}$ with binding energy $\epsilon_i = -0.5$. The phase Φ is derived from the classical action $S = \int_{t_0}^{t_\infty} L dt$ via canonical transformation [43]

$$\Phi(p_f,r_0,t_0) = \int_{t_0}^{t_\infty} L dt - p_f r(t_\infty), \tag{3}$$

where L is the system's Lagrangian (dependent on the photoelectron's trajectory $r(t)$), and $r(t_\infty)$ is the asymptotic position at $t \to \infty$ (when external fields are negligible). Mediated by the relative delay τ between the XUV and laser fields, this phase directly connects the spectrogram to the initial state, pump pulse, and probe pulse.

Optics EXPRESS

2.1.2. Gauge dependence and phase decomposition

The photoelectron phase and trajectory depend on the choice of gauge (velocity or length), which affects the description of laser-electron interactions. This gauge dependence is critical for accurately capturing experimental observables. In the velocity gauge, the Lagrangian is $L_{VG} = \dot{r}^2/2 - A_L(t) \cdot \dot{r} - V(r)$, where $A_L(t)$ is the laser vector potential and $V(r)$ is the Coulomb potential. In the length gauge, it is $L_{LG} = \dot{r}^2/2 - E_L(t) \cdot r - V(r)$, where $E_L(t) = -\partial A_L(t)/\partial t$ is the laser electric field. The phases in the two gauges are related by

$$\Phi_{LG}(p_f, r_0, t_0) = \Phi_{VG}(p_f, r_0, t_0) - A_L(t_0) \cdot r_0, \tag{4}$$

where the additional term in the length gauge depends on t_0 and r_0. As rigorously established by Silaev et al. [49], the gauge transformation multiplier connecting the length gauge to the velocity gauge incorporates the full contributions of both the XUV and the laser fields. For the XUV and laser pulse parameters we consider, the XUV field can be neglected in the gauge transformation. Specifically, we keep the XUV field intensity below 10^{12} W/cm^2 to ensure predominantly single-photon ionization, while the laser field intensity is similarly constrained to maintain perturbative dressing effects. Under these weak-field conditions, the laser field dominates the phase evolution due to its extended temporal profile, whereas the attosecond XUV pulse acts as an instantaneous ionization trigger. Tunneling ionization in strong fields predominantly occurs when $A_L(t_0) \approx 0$ (laser field maxima), where the term $A_L(t_0) \cdot r_0$ becomes negligible. This leads to accidental agreement between the two gauges at time t_0.

The phase Φ can be decomposed into two physically meaningful terms (from Eq. (3))

$$\Phi(p_f, r_0, t_0) = \int_{r_0}^{r_f} \dot{r} dr - \int_{t_0}^{t_\infty} \epsilon(t) dt, \tag{5}$$

where the first term is an adiabatic phase (integrating the kinetic momentum over the path), and the second is a dynamic phase (integrating the instantaneous total energy $\epsilon(t)$ over time). In the velocity gauge, $\epsilon_{VG}(t) = \dot{r}^2/2 + A_L(t) \cdot \dot{r} + V(r)$, while in the length gauge, $\epsilon_{LG}(t) = \dot{r}^2/2 + E_L(t) \cdot r + V(r)$. This decomposition clarifies how electron motion and energy variations contribute to the photoemission spectrum. In our model, the XUV field does not directly appear in these energy terms because its role is restricted to initiating ionization at t_0, and the subsequent dynamics governed solely by the laser field and Coulomb potential. This separation ensures the perturbative validity of our semiclassical framework under the stated intensity constraints.

Most semiclassical models in strong-field physics, including SFA, QTMC, SCTS, and CQSFA, rely on the length-gauge phase. Specifically, the phases employed in SCTS and CQSFA can be directly derived from Eq. (3) within the length gauge, reflecting their roots in classical action-based trajectories, but with limited treatment of the Coulomb-laser coupling. For the SFA, which neglects the Coulomb interaction, the length-gauge phase is expressed as

$$\Phi_{LG}^{SFA}(p_f, r_0, t_0) = -p_0 \cdot r_0 - \int_{t_0}^{t_\infty} \frac{[p_f + A_L(t)]^2}{2} dt, \tag{6}$$

where the initial momentum p_0 is unobservable. In contrast, the velocity-gauge SFA phase exposes the measurable final momentum p_f

$$\Phi_{VG}^{SFA}(p_f, r_0, t_0) = -p_f \cdot r_0 - \int_{t_0}^{t_\infty} \frac{[p_f + A_L(t)]^2}{2} dt. \tag{7}$$

The critical distinction is that length-gauge phases tie r_0 to the unobservable momentum p_0 (via $p_f = p_0 - A_L(t_0)$), while velocity-gauge phases link r_0 to the measurable momentum p_f. This is physically consistent: for two photoemission events starting at positions r_1 and r_2 with a fixed

Optics EXPRESS

offset, their detected phase difference depends on $p_f \cdot (r_1 - r_2)$ (not $p_0 \cdot (r_1 - r_2)$). In the QP model we therefore adopt the velocity gauge, ensuring consistency with experimental observables and yielding superior agreement with TDSE results (Sec. III, Figs. 2–4).

2.1.3. Path contributions

Building on the phase dynamics described earlier, the QPI model via energy conservation constrains photoelectron paths and weighs their contributions to the final spectrogram. This linkage between dynamics and energy enables a unified description of paths across different experimental techniques.

In the QPI model, trajectories of photoelectrons with a given final momentum p_f are uniquely determined by solving Newton's equations of motion subject to photoelectron interactions with the laser and Coulomb fields. For each combination of photoionization time t_0 and initial position r_0, the corresponding initial momentum p_0 is identified via an iterative search algorithm. This approach leverages a key insight: p_0 is a function of p_f, t_0, and r_0, eliminating the need for exhaustive sampling over p_0. Once the Coulomb-laser field is specified (e.g., 5 fs, 800 nm laser pulses with an intensity of 5×10^{10} W/cm^2; Fig. 1(d)), the path of a photoelectron with a given final kinetic energy $p_f^2/2$ is fully determined by t_0 and r_0, ensuring efficient yet comprehensive coverage of contributing trajectories.

Energy conservation imposes a strict constraint on the absorbed XUV photon energy, given by $\omega_X(p_f, r_0, t_0) = \frac{p_0^2}{2} + V(r_0) - \epsilon_i$, where ω_X depends explicitly on p_f, t_0, and r_0. This relation links the initial state (via ϵ_i and $V(r_0)$) and field-matter interactions (via p_0 and t_0) to the energy of the incident XUV photon, forming a critical bridge between microscopic dynamics and measurable spectral features. The joint distribution of ω_X, t_0, and r_0 for a fixed final kinetic energy [e.g., 20 eV; Fig. 1(b)] visualizes this connection: color encodes ω_X (shifted by ϵ_i), directly mapping how the XUV photon energy correlates with ionization time and initial position. This distribution reflects the combined influence of the XUV spectral amplitude [Fig. 1(a)] and the initial state probability density [Fig. 1(c)], which together determine the weight of each path in the coherent integration in the transition amplitude [Eq. (2)].

The QPI model's ability to capture ω_X-dependent path contributions enables it to unify the interpretation of streaking and RABBIT spectrograms, instead of two foundational ATRPS techniques, by clarifying their distinct XUV photon energy sensitivities. Streaking experiments use a single attosecond XUV pulse with central energy $\omega_X \approx p_f^2/2 - \epsilon_i$. Only photons near this central energy contribute to the photoelectron yield at $p_f^2/2$, as seen in the concentrated ω_X distribution [Fig. 1(a), blue solid line]. RABBIT experiments employ attosecond pulse trains (APTs) with high-order harmonics centered at $\omega_X \approx p_f^2/2 - \epsilon_i \pm \omega_L$ (where ω_L is the laser photon energy). Somewhat counterintuitively, photons near these harmonic centers do not contribute. Instead, those between and far from the centers drive the yield at $p_f^2/2$ [Fig. 1(a), green dot-dash line], with their interference encoding time-delay information.

Notably, through comprehensive analysis of all contributing paths, our model reveals that the photoemission times measured by these two techniques – despite their distinct light sources–are fundamentally defined by the τ-independent part of the phase difference between two interfering photoelectron paths. This τ-independent phase part, $\Delta\Phi$, is also independent of the specific XUV source (single pulse or pulse train) and thus corresponds to the same physical quantity, the intrinsic time delay of electron emission (Fig. 4 and Fig. 6). This finding resolves the question of why streaking and RABBIT consistently yield congruent time delay measurements, establishing their underlying unity.

By integrating dynamical trajectory calculations, energy conservation, and path coherence, the QPI model provides a comprehensive framework for quantifying how initial state properties, pump/probe fields, and spatio-temporal dynamics collectively shape attosecond time-resolved spectrograms.

Optics EXPRESS

2.2. Numerical strategy

To implement the QPI model's theoretical framework, particularly its requirement for coherent summation of all quantum paths contributing to a given final momentum $\vec{p}_f$, we develop a tailored numerical strategy. This approach addresses the limitations of traditional semiclassical methods by efficiently capturing the spatio-temporal and energetic dependencies of photoelectron trajectories

The QPI model's transition amplitude [Eqs. (1)–(2)] requires summing over all paths connecting the initial state to a final momentum $\vec{p}_f$, where each path is characterized by initial conditions $(t_0, \vec{r}_0, \vec{p}_0)$. This demand for completeness arises because quantum interference, which is critical to spectrogram features (e.g., Figs. 2–3), depends on coherent contributions from all relevant paths. Traditional semiclassical models are limited in meeting this requirement and rely on random forward sampling of t_0, $\vec{r}_0$, and $\vec{p}_0$, which may miss paths that contribute significantly to $\vec{p}_f$. Constrained by computational resources, such methods incompletely explore the configuration space, leading to errors in amplitude and phase calculations, especially for systems with complex Coulomb-laser coupling.

To resolve this, the QPI model employs retroactive path tracing, a strategy aligned with its theoretical foundation: instead of guessing initial conditions and propagating forward (as in traditional models), we work backward from $\vec{p}_f$ to identify all $(t_0, \vec{r}_0, \vec{p}_0)$ that evolve to $\vec{p}_f$. It is important to note that "retroactive" here does not imply a reverse-time integration of the equations of motion. Rather, it refers to a goal-oriented numerical strategy: starting from a fixed final momentum, we systematically search for all initial conditions that would lead to it through forward-time evolution. This ensures all physically relevant paths are included, directly implementing the model's requirement for exhaustive path summation. For linearly polarized fields and isotropic initial states, the cylindrical symmetry allows the photoemission dynamics along the polarization direction to be fully characterized by a radial coordinate treatment. For each targeted final momentum p_f, the procedure is as follows. Based on the laser pulse length and atomic structure, we sample t_0 (ionization time) and r_0 (initial position) within ranges that encompass all plausible ionization events. This step generates the spatio-temporal grid required to explore paths, as dictated by the model's phase dependence on t_0 and r_0 [Eq. (3)].

In order to estimate the initial momentum range ($[p_0^{\min}, p_0^{\max}]$), for each (t_0, r_0), we approximate the interval of initial momenta p_0, that could evolve to p_f. This range is determined via preliminary trajectory scans, ensuring it includes all p_0 consistent with energy conservation [$\omega_X \geq 0$, Eq. (2)]. Photoelectron trajectories in the coupled Coulomb-laser field obey the equation of motion

$$\frac{d^2r}{dt^2} = -E_L(t) - \frac{\partial V(r)}{\partial r}. \tag{8}$$

For each (t_0, r_0), we propagate trajectories forward, starting from $(t_0, r_0, p_0^{\min})$ and $(t_0, r_0, p_0^{\max})$ to compute their final momenta $p_f^{\min}$ and $p_f^{\max}$. Using the bisection method, we iteratively refine the interval: if $p_f^{\min}$ is closer to p_f, we set $p_0^{\max} = (p_0^{\min} + p_0^{\max})/2$, and if $p_f^{\max}$ is closer to p_f, we set $p_0^{\min} = (p_0^{\min} + p_0^{\max})/2$. The iterative search for initial momentum employs the criterion $|p_f^{\min} - p_f^{\max}| < 1.0 \times 10^{-15}$ as the convergence standard. This threshold ensures an balance between computational efficiency and numerical precision. The midpoint of the converged interval is taken as the precise p_0 for that (t_0, r_0), making sure the path satisfies the model's dynamical and energetic constraints.

This numerical strategy, tightly linked to the QPI model's theoretical structure, efficiently captures all paths contributing to p_f, enabling accurate calculations of transition amplitudes and phases. These are essential for reproducing accurate spectrograms (Figs. 2–3) and photoemission time delays (Fig. 4).

Optics EXPRESS

3. Results and discussions

3.1. Time-resolved spectrograms

To validate the accuracy of the QPI model – particularly its velocity-gauge formulation, as theoretically justified in Sec. II, we benchmark its predictions against exact results from TDSE simulations. This comparison focuses on attosecond time-resolved spectrograms obtained via both, streaking and RABBIT techniques, directly demonstrating the model's ability to capture photoelectron phase dynamics (Sec. II A).

Figures 2(a)-(c) present streaking spectrograms calculated using the TDSE, the velocity-gauge QPI model, and the length-gauge QPI model, respectively. Visually, all three spectrograms appear nearly identical, reflecting the model's qualitative correctness. However, quantitative discrepancies emerge in the residual maps [Figs. 2(d)-(e)], which compare QPI results to the exact TDSE solution. The velocity-gauge QPI model exhibits a maximum yield difference of only 2% relative to TDSE, indicating exceptional agreement. In contrast, the length-gauge QPI model shows larger deviations, with a maximum difference of 8%. This contrast aligns with our theoretical finding (Sec. II A) that the velocity gauge more accurately describes photoelectron phase, as it links spatial dependence to the measurable final momentum p_f rather than the unobservable initial momentum p_0. We further verify the temporal dynamics by examining photoelectron yields at the central energy (16.4 eV) as a function of τ. The velocity-gauge QPI model reproduces both the yield intensity and temporal shift of the TDSE result with high fidelity, while the length-gauge model shows noticeable discrepancies in both metrics.

Consistent with the streaked spectra in Fig. 2, our RABBIT spectrograms (Fig. 3) confirm the velocity-gauge QPI model's superiority. Figures 3(a)-(c) show RABBIT spectrograms from TDSE, velocity-gauge QPI, and length-gauge QPI, respectively. Residual maps [Figs. 3(d)-(e)] reveal the same pattern: 2% maximum deviation for the velocity-gauge model vs. 8% for the length-gauge model. Examination of energy-resolved temporal profiles, specifically the central mainband (25 eV) and sideband (23.4 eV), reinforces this trend: the velocity-gauge QPI model matches the TDSE results in both yield and τ-dependent shifts, while the length-gauge model deviates significantly.

These results conclusively demonstrate that the velocity-gauge QPI model accurately captures the photoelectron phase dynamics under weak-field conditions, as predicted in Sec. II. The quantitative agreement with TDSE results for both streaking and RABBIT spectra validates the model's ability to reproduce quantum interference effects, laying the groundwork for its use in interpreting spatial and temporal details of the photoemission dynamics. We note that our model does not extend to strong-field regimes, where Keldysh channel interference dominates [50,51], requiring a full quantum treatment beyond our current investigation. Thus, in the subsequent sections of this paper, our model consistently employs the velocity gauge for weak-field applications only.

3.2. Photoemission time delays

Following the validation of the QPI model in reproducing time-resolved spectrograms (Sec. III A), its superiority in calculating photoemission time delays becomes further evident. This subsection highlights three key advantages: quantum-level accuracy, computational efficiency, and the ability to unify distinct experimental techniques.

Photoemission time delays, traditionally extracted via energy integration of spectrograms and temporal shift analysis of center-of-energy (COE) traces relative to references like $-A_L(\tau)$, serve as stringent benchmarks. The velocity-gauge QPI model delivers photoemission time delays that agree with TDSE results to within 1 attosecond across a broad energy range, encompassing both streaking and RABBIT techniques [Fig. 4(a)]. This precision stems from the model's rigorous treatment of quantum phases (Sec. II A), which captures subtle Coulomb-laser coupling effects.

Optics EXPRESS

These are particularly critical at low energies, where phase interference dominates, i.e., in regime where classical models exhibit poor accuracy in time delay calculations.

The classical-trajectory Monte Carlo (CTMC) model [13], while computationally expedient for simple systems, exhibits inherent limitations in photoemission time delay calculations. Though CTMC results align with TDSE results at high energies, they deviate significantly at low energies, where quantum phase dynamics and Coulomb-laser coupling become indispensable. As a purely classical framework, the CTMC approach neglects the quantum-phase evolution, rendering it unable to reproduce interference effects foundational to RABBIT spectrograms and low-energy streaking signals. In contrast, the QPI model's explicit inclusion of quantum phases enables it to capture these effects, establishing its relevance for accurate attosecond temporal metrology. The standard eikonal approximation model [28] overestimates Coulomb-laser coupling effects for low-kinetic-energy electrons in Coulomb potentials. In our prior work, we enhanced this approach through the improved eikonal approximation (IEA) model [26], which replaces the fixed initial momentum with position-dependent momentum, a modification that substantially improves prediction accuracy. While the QPI and IEA models exhibit comparable precision in predicting photoemission time delays, the QPI framework provides a more complete physical interpretation of the underlying quantum dynamics.

The QPI model introduces a transformative approach to extracting photoemission time delays: instead of relying on time-consuming large-scale simulations of full spectrograms, time delays can be directly derived from the τ-independent phase difference ($\Delta\Phi$) between two interfering photoelectron paths. This method leverages the model's insight that all paths contributing to a final state (whether in streaking or RABBIT) belong to one of two coherent channels, with their phase difference encoding the intrinsic emission time. As shown in Fig. 4(b), time delays obtained via this phase-difference method match high-precision TDSE results, validating the model's accuracy at drastically reduced computational overhead.

3.3. Spatial and temporal encoding mechanisms in 3D photoelectron spectrograms

The preceding validation of the QPI model's accuracy in reproducing spectrograms and photoemission time delays (Secs. III A-B) lays the groundwork for dissecting the intricate encoding of differential information in 3D photoelectron spectrograms. Through analysis of the joint distribution of absorbed XUV photon energy (ω_X), photoionization time (t_0), and initial electron position (r_0) – a signature directly accessible via the QPI framework – we reveal how the XUV pump field, laser probe field, and electron initial state are coherently coupled into the spectrogram. This coupling, governed by the model's transition amplitude formalism [Eqs. (1)–(2)], enables unambiguous encoding of all relevant physical quantities.

For a fixed final kinetic energy $p_f^2/2$, the QPI model reveals that the absorbed XUV photon energy ω_X is confined to a narrow range of approximately ± 1 eV around the value $(p_f^2/2 - \epsilon_i)$, as exemplified by the tight clustering of ω_X in Figs. 5(a-c) (e.g., 20 eV final kinetic energy in Fig. 5(a) exhibits ω_X primarily between 19.4 and 20.6 eV). This constraint arises from energy conservation ($\omega_X = p_0^2/2 + V(r_0) - \epsilon_i$) and the limited energy transfer ($|\epsilon_{CL}| \lesssim 1$ eV) from the weak probe laser field, rendering the ω_X window far narrower than the full XUV spectral bandwidth [Fig. 1(a)].

To capture the complete XUV spectral information, the QPI model demonstrates that broadening the range of final kinetic energies is essential. Comparative analysis of Fig. 5(a) (20 eV) and Fig. 5(b) (10 eV) confirms that distinct final kinetic energies sample non-overlapping segments of the XUV spectrum, with their respective ω_X distributions mapping to different spectral regions of the pump field. By aggregating data across a broad kinetic energy range, the full spectral characteristics of the XUV field, including amplitude, phase, and coherence properties of single attosecond pulses or pulse trains, are coherently encoded in the 3D spectrogram via ω_X-p_f coupling.

Optics EXPRESS

The XUV pump pulse (typically sub-femtosecond in duration) is significantly shorter than the probe pulse [e.g., 5 fs as shown in Fig. 1(d)], leading to a critical temporal sampling effect: at a fixed relative delay τ, the laser field begins to interact with photoemitted electrons only after a finite time, while overlapping with the pump pulse, and thus only this time interval is encoded in the spectrogram. This phenomenon is directly evident in the t_0 distributions of Figs. 5(a-c): the laser vector potential $A_L(t_0)$ exerts the strongest modulation on the absorbed XUV photon energy ω_X at its maxima. Specifically, the variation of ω_X with t_0 in these figures aligns with the temporal profile of $A_L(t_0)$, reflecting how the laser's temporal features at discrete t_0 (corresponding to the fixed τ) couple to ω_X via energy transfer [$\epsilon_{CL} \propto A_L(t_0)$]. This alignment confirms that each fixed τ samples only a limited temporal window of the laser probe field, underscoring the need for large-range τ scanning to capture the full temporal profile of the probe field.

As τ varies, the temporal overlap window between the pump and probe pulse shifts, sampling distinct segments of $A_L(t_0)$ and thus populating complementary regions of the t_0 distribution. This is reflected in the τ-dependent modulation of streaking and RABBIT spectrograms (Figs. 2–3), where the evolving pattern across τ directly mirrors the laser's temporal amplitude and phase. Through such scanning, the 3D spectrogram accumulates the complete temporal information of the probe field, coupled to ω_X and r_0 via the phase term $\Phi(p_f, r_0, t_0)$ in the transition amplitude [Eq. (2)].

The spatial distribution of the electron initial state modulates the 3D spectrogram globally through the initial position r_0. Within the QPI model, each quantum path is weighted by the initial state probability density $r_0^2\Psi_i(r_0, t_0)$, which for the hydrogen ground state peaks at $r_0 = 1$ a.u., as shown in Fig. 1(c). This weighting ensures that paths originating from high-density regions contribute more strongly to the transition amplitude [Eq. (2)]. Critically, this weighting is not static, but couples dynamically to ω_X [via the Coulomb potential $V(r_0)$ in energy conservation] and t_0 (via the phase Φ), ensuring that spatial features of the initial state are encoded across all final kinetic energies and delays.

Collectively, these mechanisms – narrow ω_X windows per kinetic energy (expanded via p_f broadening), τ-dependent temporal sampling of the laser field, and r_0-mediated spatial weighting – ensure that 3D photoelectron spectrograms unambiguously encode all differential information: XUV pump spectrum, probe laser temporal profile, and initial state spatial distribution. Notably, current methodologies underutilize this information, focusing primarily on extracting photoemission time delays (Sec. III B) or reconstructing pump/probe temporal profiles, while neglecting the embedded spatial information [52–54].

3.4. *Unified understanding of streaking and RABBIT techniques via the QPI framework*

Building on the QPI model's ability to dissect spatiotemporal encoding in 3D spectrograms (Sec. III C), we now demonstrate how it provides a unified theoretical framework for reconciling the two primary ATRPS techniques: streaking and RABBIT. This unification reveals a common underlying mechanism rooted in quantum path interference.

RABBIT relies on weak laser-dressed single-XUV-photon excitation, a process classically described as two-color two-photon ionization: an XUV photon first excites the electron, which subsequently absorbs or emits a laser photon. From a quantum perspective, this manifests as interference between electrons excited by adjacent high-order harmonics in the XUV train, with sideband intensities modulated periodically by the relative delay τ (Fig. 3). The phase difference between these two interfering channels (absorption vs. emission of a laser photon) is traditionally expressed as $2\omega\tau - \Delta\Phi$ [2], where $\Delta\Phi$ is the τ-independent phase difference encoding the intrinsic photoemission time ($\delta\tau = \Delta\Phi/2\omega$). However, existing models struggle to calculate $\Delta\Phi$ accurately, particularly in capturing Coulomb-laser coupling effects [2,32], a limitation the QPI model overcomes.

Optics EXPRESS

The QPI model introduces a complementary semiclassical perspective, grounded in the joint distribution of ω_X, t_0, and r_0 (Fig. 5). A key constraint emerging from this framework is that, for photoelectrons with a given final kinetic energy $p_f^2/2$, only XUV photons within the energy range $p_f^2/2 \pm p_f A_{L0} \pm \delta E - \epsilon_i$ can contribute to the signal, where A_{L0} is the peak amplitude of the laser vector potential, and δE (on the order of 0.1 eV and $<<p_f A_{L0}$) accounts for subtle Coulomb-laser coupling effects [Figs. 5(d-f)]. In RABBIT experiments, the laser photon energy ω is typically much larger than $p_f A_{L0}$. Specifically, $p_f A_{L0} \approx \omega/2<\omega$ under standard experimental conditions. This inequality imposes a critical limitation: the central parts of adjacent high-order harmonics (the most intense regions of the XUV pulse train) fall outside the energy range $p_f^2/2 \pm p_f A_{L0} \pm \delta E - \epsilon_i$ (Fig. 1(a)) and thus cannot contribute to the centers of RABBIT sidebands. Instead, only the edge regions of adjacent harmonics, where the harmonic spectrum overlaps with the allowed ω_X range, participate in sideband formation. Since only the low-intensity edge regions of harmonics contribute to sidebands (in contrast to the high-intensity central regions that dominate mainbands), the intensity of RABBIT sidebands is far lower than that of mainbands.

Within this constrained framework, all paths contributing to a RABBIT sideband center can be classified into two coherent channels based on their ω_X-t_0-r_0 characteristics. While arbitrary path classifications lack physical meaning, partitioning the contributing XUV frequencies into the edge regions of two adjacent harmonics yields channels with clear physical interpretations: one channel corresponds to photoelectrons emitting a photon, and the other to absorbing a laser photon. These channels are mathematically described by $\alpha_A e^{i(\omega\tau+\Phi_A)}$ and $\alpha_B e^{i(-\omega\tau+\Phi_B)}$ (Fig. 6), where $\alpha_{A/B}$ are the amplitudes of the two channels (weak, reflecting harmonic edge contributions) and $\Phi_{A/B}$ are τ-independent phases derived from the QPI transition amplitude [Eq. (2)] [55]. The photoemission time delay emerges directly from their phase difference: $\delta\tau = (\Phi_B - \Phi_A)/2\omega$, resolving the quantitative challenge of calculating $\Delta\Phi$ [Fig. 4(b)].

For streaking, where the pump is a single attosecond XUV pulse, the QPI model reveals a direct analogy to RABBIT. By decomposing the XUV pulse's continuous frequency spectrum into two symmetric components around its central frequency ω_X^c, the interference between these components mirrors the harmonic pair interference in RABBIT. The phase difference between these symmetric channels is also modulated as $2\omega\tau - \Delta\Phi$, with $\Delta\Phi = (\Phi_B - \Phi_A)$ again encoding the same $\delta\tau$ (Fig. 6). This symmetry explains why streaking and RABBIT yield identical photoemission time delays [13]. The so-called "classical clock" (streaking) and "quantum clock" (RABBIT) are thus unified: both measure the same τ-independent phase difference $\Delta\Phi$ between interfering quantum paths, with their apparent distinction arising only from how XUV frequencies are partitioned (continuous symmetric components vs. discrete harmonics).

Notably, the QPI model predicts that photoemission time delays do not dependent on the laser intensity. As shown in Figs. 6(a)-(b), increasing laser intensity enhances the amplitudes α_A and α_B (via stronger field-dressed path contributions), but leaves the phases Φ_A and Φ_B unchanged. This invariance arises because $\Delta\Phi$ depends solely on intrinsic atomic properties (initial state, Coulomb potential) and final momentum p_f – quantities dependent of laser intensity – reinforcing the robustness of photoemission time delays as fundamental observables.

The QPI model unifies streaking and RABBIT under a single quantum path interference framework, explaining their quantitative agreement in photoemission times. Beyond this unification, the model offers a uniquely simple and efficient approach to extracting photoemission times: by directly calculating the phase difference of interfering quantum paths at any arbitrary relative delay τ, no time-consuming full spectrogram simulations or energy integration are required. Importantly, the photoemission time delays obtained via this method for both, streaking and RABBIT agree with exact TDSE results [Fig. 4(b)]. This dual merit coupled with the model's ability to decode ω_X-t_0-r_0 coupling validates the QPI model as a foundational tool for interpreting ATRPS.

Optics EXPRESS

4. Conclusion

3D attosecond time-resolved photoelectron spectrograms are currently predominantly leveraged to extract attosecond-scale temporal information, such as the characteristics of pump/probe fields and spectrally integrated photoemission time delays, while the rich differential spatial information encoded within these spectrograms remains largely untapped. To address this limitation and advance the quantitative interpretation of ATRPS, we developed the QPI model that achieves exceptional agreement with exact TDSE simulations. This model enables an in-depth dissection of ATRPS dynamics across attosecond-picometer spatiotemporal scales, resolving key ambiguities in classical and semiclassical frameworks.

A core insight of the QPI model is its revelation of how attosecond streaking and RABBIT spectrograms encode multidimensional differential information about atomic responses (initial state) and pump-probe pulse characteristics via the joint distribution of absorbed XUV photon energy ω_X, photoionization time t_0, and initial electron position r_0 for photoelectrons with identical final kinetic energies. Unlike simplistic direct mappings, this joint distribution coherently couples the XUV pump field (via ω_X spectral modulation), probe laser field [via t_0-dependent interaction with the laser vector potential $A_L(t_0)$], and initial state probability density (via r_0-weighted path contributions; Fig. 5). This coupling mechanism not only unifies the “classical clock" (streaking) and “quantum clock" (RABBIT) paradigms, demonstrating that both techniques derive photoemission times from the same τ-independent phase difference of interfering quantum paths, but also enables efficient extraction of emission times at any arbitrary τ (without time-consuming full spectrogram simulations), with results that are fully consistent with *ab initio* TDSE calculation.

While initial state probability density and Coulomb-laser coupling effects are naturally incorporated into the QPI model, current algorithms for retrieving pump and probe fields often neglect these factors [52–54], leading to degraded accuracy in reconstructed field profiles. Probing and controlling subatomic ultrafast dynamics demands imaging techniques that integrate attosecond temporal resolution with picometer spatial resolution–a capability lacking in current ultrafast imaging methods, which typically sacrifice spatial resolution for temporal precision. The QPI model fills this gap by providing a rigorous physical framework for fully exploiting 3D spectrograms: it enables simultaneous imaging of the XUV pump field, laser probe field, and initial electron state at attosecond-picometer resolution, provided advanced reconstruction algorithms tailored to its coupling rules are developed.

A critical challenge in realizing this potential lies in reconstructing the 3D differential information (temporal: pump/probe fields; spatial: initial state) from 3D spectrograms using traditional algorithms. While retrieving pump/probe field temporal profiles is relatively straightforward, extracting the initial-state probability density is far more complex. This quantity influences only the finer details of spectrograms, making it difficult to isolate via conventional inversion methods. To address this, we propose the future development of self-supervised deep neural network-based reconstruction algorithms [56–58]. Employing iterative generative models subject to the QPI model’s physical constraints (e.g., energy conservation, ω_X-t_0-r_0 coupling), such algorithms can circumvent the need for extensive training datasets while ensuring physically meaningful reconstructions.

Funding. National Natural Science Foundation of China (12174295, 11934006, 12104349); Natural Science Foundation of Hubei Province, China (2020CFA082); U.S. National Science Foundation (PHY 2409183); Office of Basic Energy Sciences (DEFG02-86ER13491).

Disclosures. There are no conflicts of interest to declare.

Data availability. Data underlying the results presented in this paper are not publicly available at this time but may be obtained from the authors upon reasonable request.

Optics EXPRESS

References

1. M. Schultze, M. Fieß, N. Karpowicz, *et al.*, "Delay in photo-emission," Science **328**(5986), 1658–1662 (2010).
2. K. Klünder, J. M. Dahlström, M. Gisselbrecht, *et al.*, "Probing Single-Photon Ionization on the Attosecond Time Scale," Phys. Rev. Lett. **106**(14), 143002 (2011).
3. Z. Tao, C. Chen, T. Szilvási, *et al.*, "Direct time-domain observation of attosecond final-state lifetimes in photoemission from solids," Science **353**(6294), 62–67 (2016).
4. M. Ossiander, F. Siegrist, V. Shirvanyan, *et al.*, "Attosecond correlated dynamics," Nat. Phys. **13**(3), 280–285 (2017).
5. M. Isinger, R. J. Squibb, D. Busto, *et al.*, "Photo-ionization in the time and frequency domain," Science **358**(6365), 893–896 (2017).
6. F. Siek, S. Neb, P. Bartz, *et al.*, "Angular momentum-induced delays in solid-state photoemission enhanced by intra-atomic interactions," Science **357**(6357), 1274–1277 (2017).
7. J. Vos, L. Cattaneo, S. Patchkovskii, *et al.*, "Orientation-dependent stereo Wigner time delay and electron localization in a small molecule," Science **360**(6395), 1326–1330 (2018).
8. J. Fuchs, N. Douguet, S. Donsa, *et al.*, "Time delays from one-photon transitions in the continuum," Optica **7**(2), 154 (2020).
9. H. Shi and U. Thumm, "Photoelectron–residual-ion interaction in angle-resolved streaked shake-up ionization of helium," Phys. Rev. A **111**(1), 013119 (2025).
10. L. Cattaneo, J. Vos, M. Lucchini, *et al.*, "Comparison of attosecond streaking and RABBITT," Opt. Express **24**(25), 29060 (2016).
11. M. Sabbar, S. Heuser, R. Boge, *et al.*, "Resonance effects in photoemission time delays," Phys. Rev. Lett. **119**(21), 219901 (2017).
12. E. P. Wigner, "Lower limit for the energy derivative of the scattering phase shift," Phys. Rev. **98**(1), 145–147 (1955).
13. R. Pazourek, S. Nagele, and J. Burgdörfer, "Attosecond chronoscopy of photoemission," Rev. Mod. Phys. **87**(3), 765–802 (2015).
14. M. Huppert, I. Jordan, D. Baykusheva, *et al.*, "Attosecond delays in molecular photoionization," Phys. Rev. Lett. **117**(9), 093001 (2016).
15. S. Haessler, B. Fabre, J. Higuet, *et al.*, "Phase-resolved attosecond near-threshold photoionization of molecular nitrogen," Phys. Rev. A **80**(1), 011404 (2009).
16. L. Cattaneo, J. Vos, R. Y. Bello, *et al.*, "Attosecond coupled electron and nuclear dynamics in dissociative ionization of H_2," Nat. Phys. **14**(7), 733–738 (2018).
17. C. Marceau, V. Makhija, D. Platzer, *et al.*, "Molecular frame reconstruction using time-domain photoionization interferometry," Phys. Rev. Lett. **119**(8), 083401 (2017).
18. P. Hockett, E. Frumker, D. M. Villeneuve, *et al.*, "Time delay in molecular photoionization," J. Phys. B At. Mol. Opt. Phys. **49**(9), 095602 (2016).
19. I. A. Ivanov, A. S. Kheifets, and V. V. Serov, "Attosecond time-delay spectroscopy of the hydrogen molecule," Phys. Rev. A **86**(6), 063422 (2012).
20. V. V. Serov, V. L. Derbov, and T. Sergeeva, "Interpretation of time delay in the ionization of two-center systems," Phys. Rev. A **87**(6), 063414 (2013).
21. V. V. Serov, A. S. Kheifets, and J. Chem, "Time delay in XUV/IR photoionization of H_2O," Phys. **147**(20), 204303 (2017).
22. P. Hockett, "Angle-resolved RABBITT: theory and numerics," J. Phys. B At. Mol. Opt. Phys. **50**(15), 154002 (2017).
23. G. Sansone, F. Kelkensberg, J. F. Pérez-Torres, *et al.*, "Electron localization following attosecond molecular photoionization," Nature **465**(7299), 763–766 (2010).
24. Ch. Neidel, J. Klei, C.-H. Yang, *et al.*, "Probing time-dependent molecular dipoles on the attosecond time scale," Phys. Rev. Lett. **111**(3), 033001 (2013).
25. D. Kiesewetter, R. R. Jones, A. Camper, *et al.*, "Probing electronic binding potentials with attosecond photoelectron wavepackets," Nat. Phys. **14**(1), 68–73 (2018).
26. F. Wang, Q. Liao, K. Liu, *et al.*, "Determination of the photoemission position in single-photon ionization with attosecond streaking spectroscopy," Phys. Rev. A **103**(1), 013115 (2021).
27. U. Thumm, Q. Liao, E. M. Bothschafter, *et al.*, in *Handbook of Photonics Vol. 1: Attosecond Physics*, D. L. Andrew, ed. (Wiley, 2015).
28. C.-H. Zhang and U. Thumm, "Electron-ion interaction effects in attosecond time-resolved photoelectron spectra," Phys. Rev. A **82**(4), 043405 (2010).
29. M. Ivanov and O. Smirnova, "How Accurate is the Attosecond Streak Camera?" Phys. Rev. Lett. **107**(21), 213605 (2011).
30. S. Nagele, R. Pazourek, J. Feist, *et al.*, "Time-resolved photoemission by attosecond streaking: extraction of time information," J. Phys. B: At., Mol. Opt. Phys. **44**(8), 081001 (2011).
31. J. M. Dahlström, D. Guénot, K. Klünder, *et al.*, "Theory of attosecond delays in laser-assisted photo-ionization," Chem. Phys. **414**, 53–64 (2013).
32. A. Maquet, J. Caillat, and R. Taïeb, "Attosecond delays in photo-ionization: Time and quantum mechanics," J. Phys. B **47**(20), 204004 (2014).
33. U. Saalmann and J. M. Rost, "Proper Time Delays Measured by Optical Streaking," Phys. Rev. Lett. **125**(11), 113202 (2020).

Optics EXPRESS

34. L. V. Keldysh, "Ionization in the field of a strong electromagnetic wave," Zh. Eksp. Teor. Fiz. **47**, 1945 (1964).
35. F. H. M. Faisal, "Multiple absorption of laser photons by atoms," J. Phys. B.: At. Mol. Opt. Phys. **6**(4), L89–L92 (1973).
36. H. R. Reiss, "Effect of an intense electromagnetic field on a weakly bound system," Phys. Rev. A **22**(5), 1786–1813 (1980).
37. S. V. Popruzhenko and D. Bauer, "Strong field approximation for systems with Coulomb interaction," J. Mod. Opt. **55**(16), 2573–2589 (2008).
38. S. V. Popruzhenko, G. G. Paulus, and D. Bauer, "Coulomb-corrected quantum trajectories in strong-field ionization," Phys. Rev. A **77**(5), 053409 (2008).
39. T.-M. Yan, S. V. Popruzhenko, M. J. J. Vrakking, *et al.*, "Low-Energy Structures in Strong Field Ionization Revealed by Quantum Orbits," Phys. Rev. Lett. **105**(25), 253002 (2010).
40. X.-Y. Lai, C. Poli, H. Schomerus, *et al.*, "Influence of the Coulomb potential on above-threshold ionization: A quantum-orbit analysis beyond the strong-field approximation," Phys. Rev. A **92**(4), 043407 (2015).
41. X. Lai, S. Yu, Y. Huang, *et al.*, "Near-threshold photoelectron holography beyond the strong-field approximation," Phys. Rev. A **96**(1), 013414 (2017).
42. M. Li, J. Geng, H. Liu, *et al.*, "Classical-quantum correspondence for above-threshold ionization," Phys. Rev. Lett. **112**(11), 113002 (2014).
43. N. I. Shvetsov-Shilovski, M. Lein, L. B. Madsen, *et al.*, "Semiclassical two-step model for strong-field ionization," Phys. Rev. A **94**(1), 013415 (2016).
44. J. Li and U. Thumm, "A semiclassical approach for solving the time-dependent Schrödinger equation in inhomogeneous pulses of electromagnetic radiation," Phys. Rev. A **101**(1), 013411 (2020).
45. F. Navarrete, M. F. Ciappina, and U. Thumm, "Crystal-momentum-resolved contributions to high-order harmonic generation in solids," Phys. Rev. A **100**(3), 033405 (2019).
46. M. He, Y. Li, Y. Zhou, *et al.*, "Direct visualization of valence electron motion using strong-field photoelectron holography," Phys. Rev. Lett. **120**(13), 133204 (2018).
47. J. Tan, Y. Zhou, M. He, *et al.*, "Determination of the ionization time using attosecond photoelectron interferometry," Phys. Rev. Lett. **121**(25), 253203 (2018).
48. C.-H. Zhang and U. Thumm, "Attosecond Photoelectron Spectroscopy of Metal Surfaces," Phys. Rev. Lett. **102**(12), 123601 (2009).
49. A. A. Silaev, A. A. Romanov, M. V. Silaeva, *et al.*, "Second-order imaginary differential operator for effective absorption in the numerical solution of the time-dependent Schrödinger equation," Phys. Rev. A **108**(1), 013118 (2023).
50. A. A. Romanov, T. S. Sarantseva, A. V. Sviridov, *et al.*, "Streaking camera in the high intensity regime," Opt. Lett. **49**(4), 1037 (2024).
51. A. V. Sviridov, T. S. Sarantseva, A. A. Romanov, *et al.*, "Streaking camera for a high-intensity infrared laser field," Phys. Rev. A **110**(6), 063103 (2024).
52. G. Sansone, E. Benedetti, F. Calegari, *et al.*, "Isolated Single-Cycle Attosecond Pulses," Science **314**(5798), 443–446 (2006).
53. J. Gagnon, E. Goulielmakis, and V. S. Yakovlev, "The accurate FROG characterization of attosecond pulses from streaking measurements," Appl. Phys. B **92**(1), 25–32 (2008).
54. V. S. Yakovlev, J. Gagnon, N. Karpowicz, *et al.*, "Attosecond Streaking Enables the Measurement of Quantum Phase," Phys. Rev. Lett. **105**(7), 073001 (2010).
55. Q. Liao, W. Cao, Q. Zhang, *et al.*, "Distinction of Electron Dispersion in Time-Resolved Photoemission Spectroscopy," Phys. Rev. Lett. **125**(4), 043201 (2020).
56. L. Qu, S. Zhao, Y. Huang, *et al.*, "Self-inspired learning for denoising live-cell super-resolution microscopy," Nat. Methods **21**(10), 1895–1908 (2024).
57. X. Chen, C. Qiao, T. Jiang, *et al.*, "Self-supervised denoising for multimodal structured illumination microscopy enables long-term super-resolution live-cell imaging," PhotoniX **5**(1), 4 (2024).
58. T. Liu, Y. Quan, Y. Su, *et al.*, "Astronomical image denoising by self-supervised deep learning and restoration processes," Nat. Astron. **9**(4), 608–615 (2025).